Int. J. Electrochem. Sci., 14 **(2019)** 1461 – 1478, doi: 10.20964/2019.02.04

International Journal of
ELECTROCHEMICAL
SCIENCE
www.electrochemsci.org

Morphological and Optical Properties of SnO_2 Doped ZnO Nanocomposites for Electrochemical Sensing of Hydrazine

Atif Mossad Ali[1,2,*], *Omniat Qreshah*[3], *Adel A. Ismail*[4],*Farid A. Harraz*[4,5], *Hamed Algarni*[1],
Mohammed A. Assiri[6], *Mohd Faisal*[5], *Wee Siong Chiu*[7]

[1] Department of Physics, Faculty of Science, King Khalid University, Abha, Saudi Arabia
[2] Department of Physics, Faculty of Science, Assiut University, Assiut, Egypt
[3] Physics Department, Faculty of Arts & Science, Najran University, Saudi Arabia
[4] Central Metallurgical Research and Development Institute, Helwan, Cairo, Egypt
[5] Promising Centre for Sensors and Electronic Devices, Najran University, Najran, Saudi Arabia
[6] Department of Chemistry, Faculty of Science, King Khalid University, Abha, Saudi Arabia
[7] Low Dimensional Materials Research Centre, Department of Physics, Faculty of Science, University of Malaya, Kuala Lumpur, Malaysia
[*]E-mail: atifali@kku.edu.sa

Received: 14 July 2018 / *Accepted:* 21 November 2018 / *Published:* 5 January 2019

SnO_2/ZnO nanomaterials were synthesized by sol-gel method using polyethylene glycol with different SnO_2 contents. The synthesized samples were annealed at 600 °C. The effects of SnO_2/ZnO were investigated Viz., molar ratios, morphology, optical and photocatalytic properties. The prepared samples were analyzed by XRD, TEM, SEM, FT-Raman spectroscopy, N_2 physical adsorption, FT-IR, and UV-Vis spectroscopy. The optical band gaps of SnO_2/ZnO nanocomposites were obtained from UV-diffuse reflectance spectroscopic studies. The photocatalytic activities of prepared samples increased with the decrease SnO_2 content, which could be explained by increase in charge parting resulting from the coupling of ZnO with SnO_2 due change in potential energy. Additionally, the SnO_2/ZnO nanocomposite with the optimal molar ratio was used to change a glassy carbon electrode (GCE) and then employed successfully for the electrochemical sensing of hydrazine at various concentrations using the amperometric technique. The modified GCE showed high sensitivity 1.16 $\mu A \mu M^{-1} cm^{-2}$, linear dynamic range 2.5 to 25µM ($R^2 = 0.9997$), fast response time within 5s and a limit of detection (LOD) 0.36 µM at (*S/N*=3).

Keywords: Electrochemical sensing; Cyclic voltammetry; SnO_2/ZnO ; Nanocomposites ; Sol-gel ; Photocatalytic degradation

1. INTRODUCTION

Metal oxide semiconductors have found huge importance in the field modern era [1]. It shows wide verity of applications in sensors and devices [2]. They also provide a good platform to modify various physical properties due to their small size and a high density of surface. The structural, optical, and electronic properties are determined by the particle size [3,4].

SnO_2 and ZnO are belonging to n-type with band gap of 3.6 and 3.37 eV, respectively [5]. SnO_2/ZnO nanocomposites shows a high electron conductivity, mobility, and found large usage in transparent electrodes for solar cells [6], anode materials [7], sensors [8], field emission devices, optoelectronic devices [9-11], and photocatalysts [12]. There are several techniques to prepare SnO_2/ZnO nanocomposites including magnetron sputtering [13,14], sol-gel [15], and hydrothermal and PLD [16].

Among these methods, the sol-gel method provide many benefits compare to other methods such as low processing temperature, low cost, better homogeneity, high purity of products, and controlled stoichiometry [17]. This technique epitomizes way of preparation and gives tremendous properties appropriate for many applications. In view of this, wide verities of catalyst agents or catalysts have been prepared by this method [18-21]. SnO_2-based gas sensor devices can be used to detect various inflammable and harmful gases such as hydrogen, carbon monoxide, ethanol, and methanol [22]. ZnO is a versatile material due to its various physical properties [23, 24]. It can also used as a sensor, energy conversion, energy generator, and photocatalyst in hydrogen production owing to its piezo- and pyroelectric properties [25, 26].

The photocatalytic method produces redox reactions with the material absorbed on the surface of the photocatalyst by the formation of electron-hole pairs by means of band-gap radiation. However, a very high degree of photogenerated holes and electrons recombination in the semiconductors decrease their photocatalytic efficiency and in the deprivation of impurities in air and water [27]. The process of the photocatalysis is growing the charge separation and its photocatalytic efficiency. Providentially, the process of doping in band-gap energy can increase the charge departure and enlarge photocatalytic activity for phase reactions than the single semiconductor photocatalysts [28-31]. The current work is focused on the synthesize of SnO_2/ZnO nanocomposites in presence of polyethylene glycol (PEG) and the consequence of SnO_2 on the structural, optical, and the photocatalytic properties. In addition, The SnO_2/ZnO nanocomposite was used to change glassy carbon electrode and applied for the electrochemical sensing of hydrazine. In our previous work [32], 0.1 SnO_2/1.0 ZnO was synthesized by sol-gel method and annealed at 600 ^oC was used for the electrochemical sensing of liquid ethanol.

2. EXPERIMENTAL

2.1 Samples synthesis

SnO_2/ZnO nanocomposites were prepared by sol-gel method. In a beaker, 1.0 gm of polyethylene glycol (PEG) was dissolved in 100 mL H_2O and then $Zn(CH_3COO)_2 \cdot 2H_2O$ and preferred quantity of tetrachloride 5-hydrate ($SnCl_4.5H_2O$) were subsequently mixed to the PEG with vigorous magnetic stirring for 2 h. Then, the as-prepared nanocomposites were dehydrated at 120 ^oC for 24 h and the samples were annealed at 600 ^oC for 4 h. The molar ratios of SnO_2/ZnO prepared samples are 1.0:1.0, 0.5:1.0, 0.3:1.0, and 0.1:1.0, respectively.

2.2 Characterization

The XRD studies of prepared material were characterized by SHIMADZU XD-D1. The spectral studies of all the samples were measured using Perkin Elmer Raman Station 400. The surface topography of the all the materials were examined using a SEM (JSM 6360 LA, Japan). FTIR spectroscopy (Perkin Elmer) was employed to understand the vibrational spectra. The optical data was measured using a UV/Vis spectrometer. The TEM data of prepared samples was recorded by A JEM–2100F. The Nitrogen adsorption-desorption isotherms were measured by NOVA2000e instrument.

2.3 Photocatalytic method

The photocatalytic test of different content of SnO_2 in SnO_2/ZnO was performed using methylene blue as a probe molecule. The experiment is conducted using a 100 mL container fitted with 250 W lamp (visible) placed on a magnetic stirrer. After that a suspension of 1 g/L of prepared nanostructures of methylene blue (0.02 mM) was nonstop stirred for 2 h in dark to get adsorption equilibrium. After that the solution aerated to oxygen supply throughout investigates. The preapared samples were removed at regular interval and centrifuged. The methylene blue elimination was studied by calculating the change in the absorbance at 663 nm wavelength of MB using a UV–visible spectrophotometer.

2.4 Electrochemical Sensing of Hydrazine

The prepared material with optimal molar ratio 0.1 SnO_2/1.0 ZnO was used to change glassy carbon electrode for the electrochemical sensing of hydrazine. The GCE with a surface area 0.071 cm^{-2} was initially polished by 1µm and 0.05 µm diamond and alumina slurry. The active SnO_2/ZnO nanocomposite was smoothly mixed with a butyl carbitol acetate/ethyl acetate binder and then coated onto the GCE. Electrode drying was carried out at ~65 ^oC for 5 h. Zahner Zennium electrochemical workstation was connected to a three electrode system for both cyclic voltammetric and amperometric measurements. GCE modified by SnO_2/ZnO is the working electrode, while a Pt wire is a counter electrode, and Ag/AgCl is the reference electrode. The electrochemical measurements were conducted in phosphate buffer solution (PBS) of pH=7.4.

3. RESULTS and DISCUSSION

XRD graphs of SnO_2/ZnO nanocomposites by sol-gel method and annealed at 600 ^oC with different SnO_2 contents are illustrated in Fig. 1. As shown in this diagram, sharp peaks at $2\theta = 26.5^o$, 33.95^o, and 36.19^o due to SnO_2 (110), ZnO (002), and ZnO (101), respectively, were observed. The intensity of the first peak (SnO_2 (110)) decreases with a decrease in the SnO_2 concentration. Conversely, the intensity of the third peak (ZnO (101)) increases with the decrease in SnO_2 content, i.e., an increase in ZnO content. Additionally, the intensity of second peak (ZnO (002)) remains almost the same. These results indicate that high orientation occurs in the (110), (002) and (101) planes, which concords well with the results obtained by Khodami and Ejhieh [33]. The patterns of SnO_2/ZnO nanocomposites display representative SnO_2 peaks centered at $2\theta = 51.82^o$ and 54.70^o due to the (211) and (220) planes, respectively. In addition, ZnO peaks at $2\theta = 47.5^o$ and 56.5^o are due to the (102) and (110) planes, respectively. The crystal size of SnO_2/ZnO nanocomposites was quantitatively determined based on Scherrer's formula $D = K\lambda/B\cos\theta$ [34], where all the notations have their usual meanings., the mean size (D) of the crystal grains were calculated from SnO_2 (110) to be 10.2 nm, 12.4 nm, 19.4 nm, and 24.3 nm and from ZnO (002) to be 34.5 nm, 31.4 nm, 27.7 nm, and 24 .4 nm for the SnO_2/ZnO nanocomposites prepared at 1.0:1.0, 0.5:1.0, 0.3:1.0 and 0.1:1.0 molar ratios, respectively, as shown in Fig. 2.

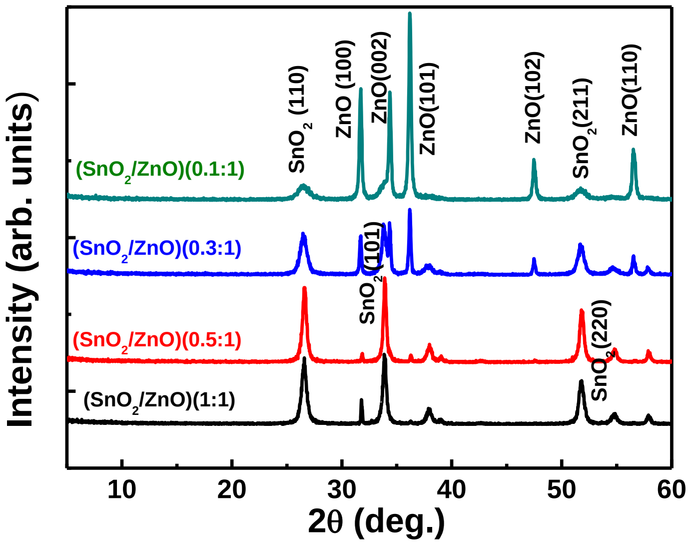

Figure 1. XRD patternS of SnO_2/ZnO annealed at 600 °C.

FTIR spectroscopy was measured for quantitative and qualitative analysis of the chemical bonds in the samples. As shown in Fig. 3, the observed peaks at 570 cm^{-1} and 670 cm^{-1} are attributed to Zn-O bonds [35] and O-Sn-O lattice [36], respectively. The intensities of the Zn-O bonds decrease and those of O-Sn-O lattice increase with increasing SnO_2. The weak peak at 1650 cm^{-1} is related to symmetric C=O bond vibrations. Very weak peaks situated at 2380 cm^{-1} and 2850 cm^{-1} could be attributed to the absorption of CO_2 and hydroxyl groups of water molecules, respectively, due to atmospheric moisture. This outcome suggests that the quality (low impurities) of the SnO_2/ZnO nanocomposites is very high.

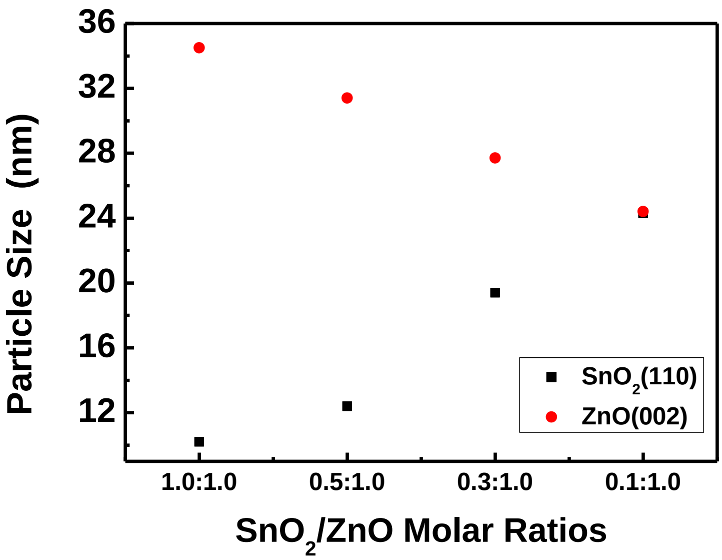

Figure 2. The particle size (D) of SnO_2/ZnO nanocomposites annealed at 600 °C.

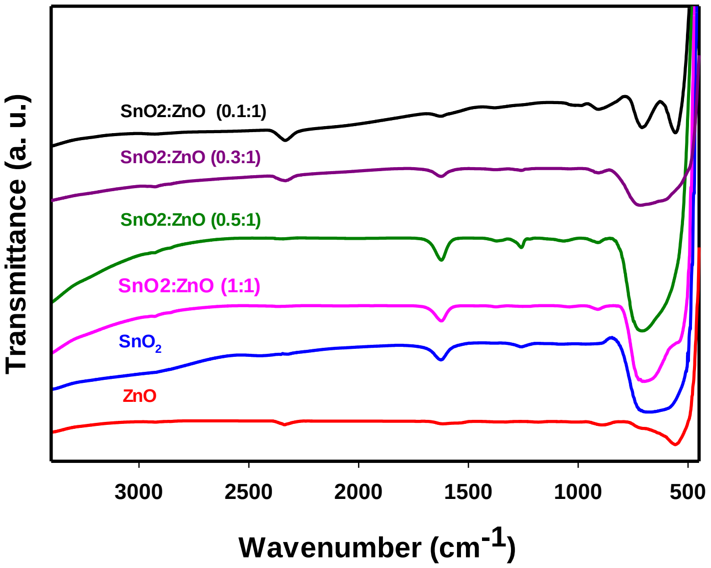

Figure 3. FTIR of SnO_2/ZnO nanocomposites annealed at 600 °C.

From the literature the Raman modes for ZnO are $A_1 + 2E_2 + E_1$, where A_1 and E_1 represents polar phonons and, they exhibit different frequencies for the TO and LO phonons. Similarly the Non-polar phonon E_2 have two frequencies like E_2 (high) related with oxygen atoms and E_2 (low) related with Zn sublattice [37]. In addition, SnO_2 exhibit a tetragonal rutile structure with point group 14. Some reports already reported the mechanical representation of the normal vibration modes at the center of the Brillouin zones as[38, 39]:

$$\Gamma = 1A_{1g}+1A_{2g}+1A_{2u}+1B_{1g}+1B_{2g}+2B_{1u}+1E_g+3E_u \qquad (1)$$

Fig. 4 shows the vibrational modes of the prepared nanocomposites. The spectra consists several characteristics vibrational modes of SnO_2 and ZnO at 468, 652, and 721 cm^{-1} are attributed to the E_g, A_{1g}, and B_{2g} of SnO_2, respectively [40]. The E_2H-E_2L, A_1 (TO), E_2 (high) and E_1 (LO) vibrational modes of ZnO are assigned to 332, 377, 438, 591 cm^{-1} respectively [41]. The peaks at 857 and 891 cm^{-1} for hexagonal ZnO arise for modes (LA to TO) and 2TO.

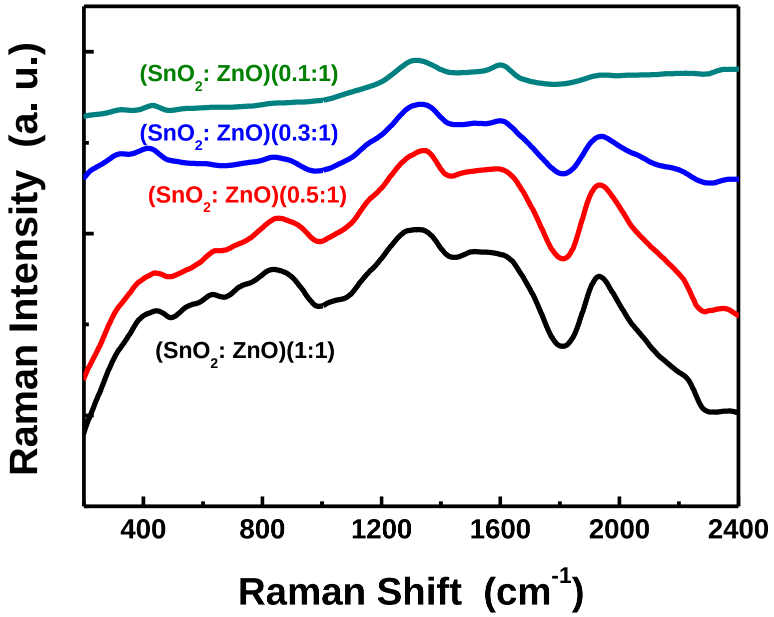

Figure 4. Raman spectroscopy of SnO2/ZnO.

SEM is a unique method to analyze the morphology of the synthesized nanocomposites. Fig. 5 shows the SEM micrographs of the SnO_2/ZnO nanocomposites. The as-synthesized SnO_2/ZnO nanocomposites consist of grains and nanorods. As shown in Fig. 5(a), a pure ZnO sample has agglomerated type of morphology and the grains attached to each other and form a cluster but the pure SnO_2 sample shows nanorods morphology (Fig. 5(b)). SnO_2/ZnO nanorods are collected of polycrystalline hexagonal wurtzite ZnO and rutile SnO_2 (Figs. 5(c) and (d)). The numbers of the nanorods decrease with the decreasing SnO_2 content.

The topography of the prepared pure SnO_2, ZnO, and SnO_2/ZnO nanocomposites were distinguished by TEM. Fig. 6(a) shows a representative TEM image of the pure SnO_2 nanorods growing at a high density with a random distribution. As shown in the images, the rods are not of homogeneous size and vary from 20 nm to 100 nm in length and 20 nm in diameter. The high resolution (HR) TEM image and its equivalent FFT designate the single crystalline nature (Fig. 6(b)). The gap between adjoining lattice planes parallel to the growth direction is 0.33 nm. The preferential growth of the SnO_2

nanorods occurs along the normal of (110) planes. Fig. 6(c) shows a TEM image of pure ZnO powder. The particle morphology is spherical as a result of PEG addition.

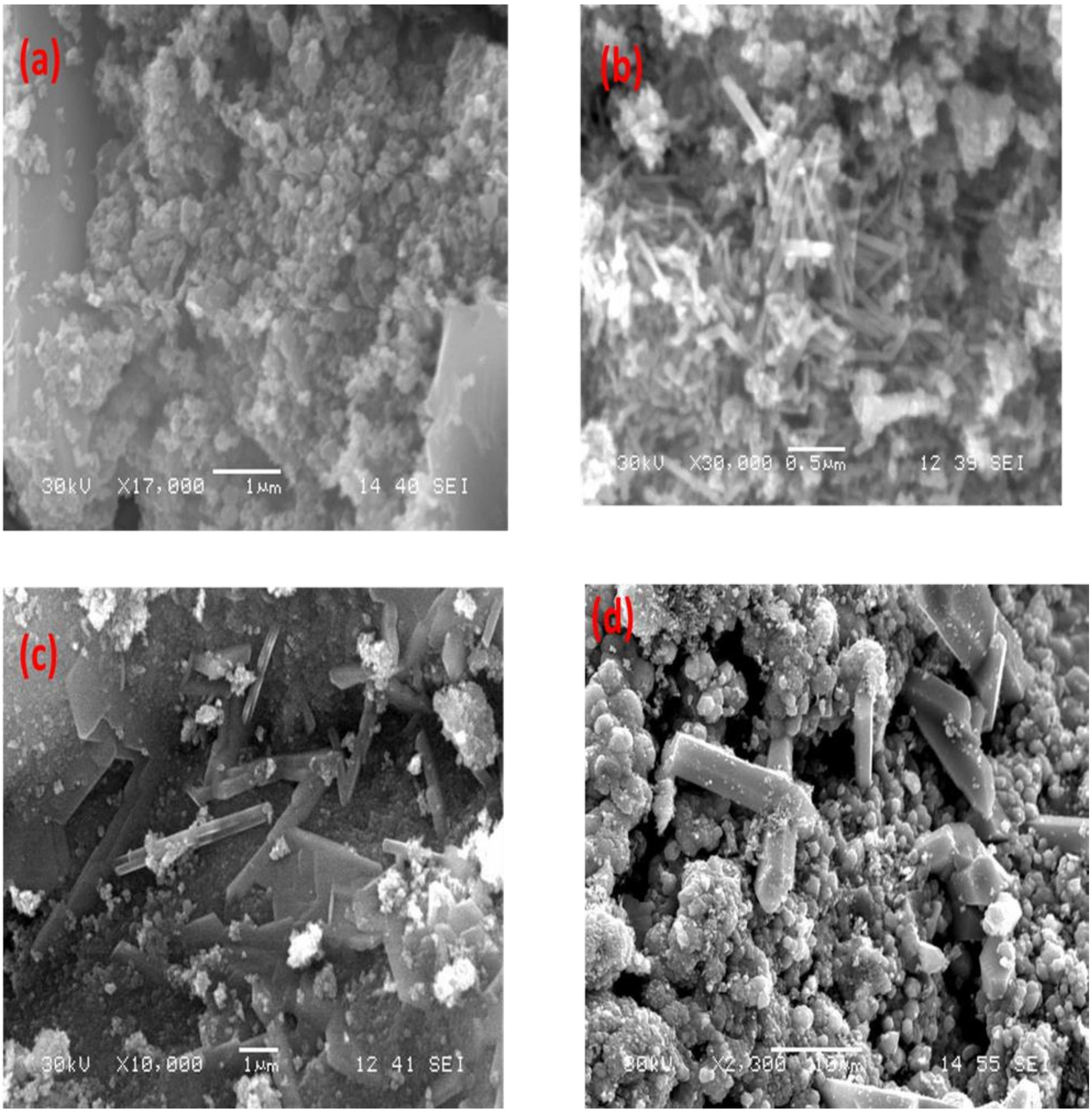

Figure 5. SEM images of pure ZnO (a), pure SnO_2 (b), SnO_2/ZnO nanocomposite [1.0:1.0] (c) and SnO_2/ZnO nanocomposite [0.1:1.0] (d).

The interfacial structure of the prepared samples was identified by the HRTEM observation as presented in Fig. 6(d). It clearly shows that SnO_2/ZnO has a nanorod structure similar to that of SnO_2. The SnO_2/ZnO nanorod units possess a hexagonal end face and span from 30 to 50 nm with a diameter of about 10–15 nm (Fig. 6(d)). The chosen area electron diffraction (SAED) patterns for SnO_2/ZnO shows numerous bright concentric rings, as shown in Fig. 6(d). The inset of the figure suggests that the studied materials showing a polycrystalline structure corresponding to various diffraction planes of tetragonal polycrystalline SnO_2. It can be inferred that PEG likely serves as a structure-directing agent for scheming the formation of SnO_2/ZnO nanocomposites. It indicates that Zn is effecting the morphology of SnO_2 nanostructure.

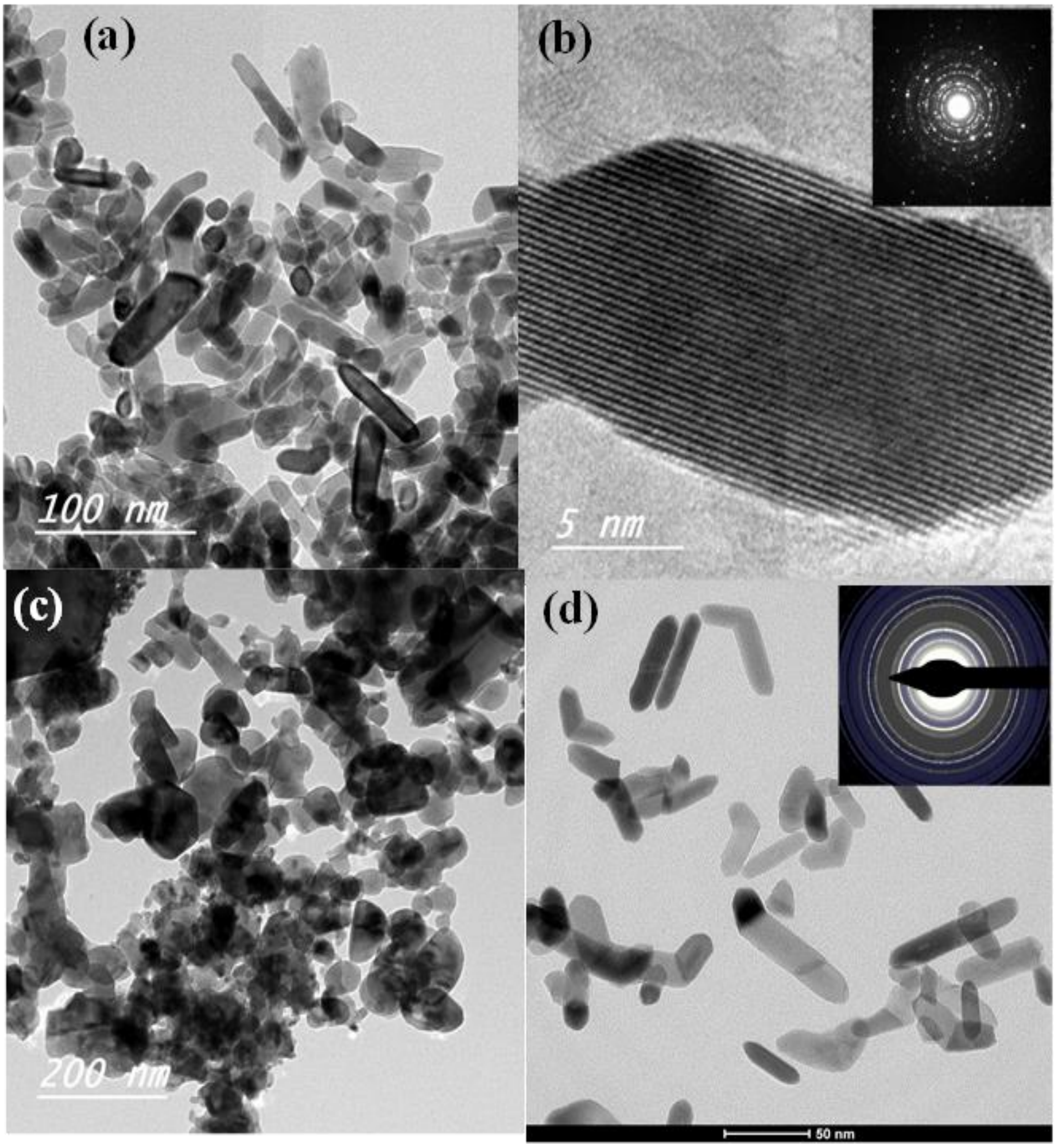

Figure 6. TEM images of pure SnO_2 (a), HRTEM image of pure SnO_2 (b) and its corresponding FFT designate the single crystalline nature (inset). TEM image of pure ZnO powder (c), and HRTEM of the interfacial structure of the SnO_2/ZnO (0.1:1.0) nanocomposite (d). SAED arrangements for SnO_2/ZnO exhibit several bright concentric rings, as shown in Fig. 6 (d) (inset).

The DR spectra of SnO_2/ZnO nanocomposites at different SnO_2 contents are carried out in diffuse reflectance mode (R) using the Kubelka-Munk function F(R) and the plots are shown in Fig. 7.

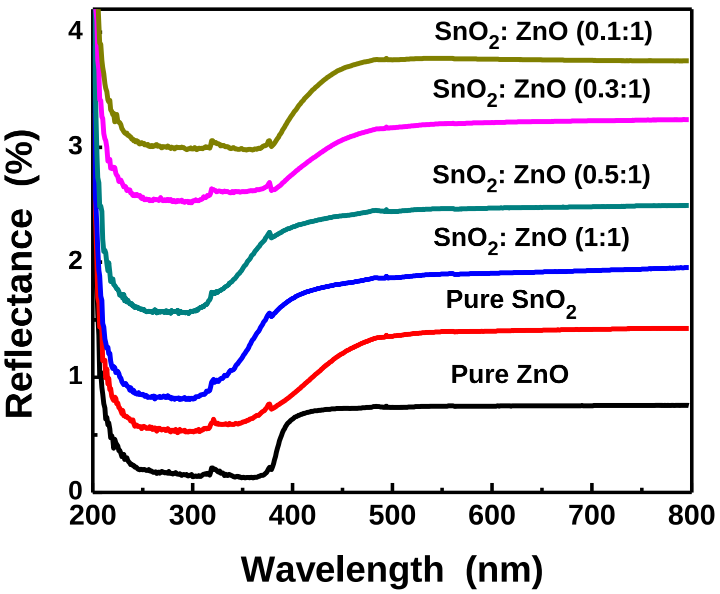

Figure 7. DR spectra of undoped (pure ZnO and pure SnO_2) and SnO_2 doped ZnO nanocomposites.

The band gap values calculated from Kubelka-Munk function [42] as shown in Fig. 8.

$$F(R)E^{1/2} = [(1-R)^2 h\nu]^{1/2} \qquad (2)$$

where *h* and υ have their usual meanings. The measured band gap of pure SnO_2 nanoparticles is 3.20 eV, which is lower than the earliear reported values i.e., 3.6 eV [43,44]. The band gaps of SnO_2/ZnO nanocomposite (1.0:1.0) and SnO_2/ZnO nanocomposite (0.1:1.0) are 3.5 and 3.0 eV, respectively. The E_g values are decrease with the decreasing SnO_2 contents with the increase in particle size (Fig. 2).

Fig.9 shows the time-dependent UV-Vis micrograph of methylene blue under UV light. The Three absorption bands, 245 nm, 291 nm and 663 nm for methylene blue MB dye, slowly decrease with the rise in the irradiation times. To form leuco-MB there are two processes are adopted either by two-electron reduction to its colorless form or oxidative degradation or [42]. Further, the absence band at 245 nm of leuco-MB indicates the decoloration of MB is due to the oxidative degradation of the dye in the presence of a photocatalyst.

Fig.10 indicates the change in the degradation rate with decreasing SnO_2 contents. The order of photocatalytic performance is 0.1 SnO_2:1.0 ZnO > 0.3 SnO_2:1.0 ZnO > 0.5 SnO_2:1.0 ZnO > 1.0 SnO_2:1.0 ZnO, suggesting that doping of SnO_2 increase the photocatalytic reaction of ZnO. The reason could be explained due to increase the photocatalytic reaction of SnO_2/ZnO by the creation of heterojunctions between SnO_2 and ZnO, which may controlling the electron/ hole pair recombination and increase their number. As a result hydroxyl radicals ($OH^{\bullet}$) and superoxide radical anions ($O_2^{\bullet -}$), are drive the photodegradation or mineralization of the dye molecule. The reason for the formation of heterojunctions can be attributed to that the ionic radius of Sn^{4+} is equal to that of Zn^{+2} [45] and the mutual action of both oxides results in the suppression of photogenerated electron and hole recombination, which increases photocatalysis [45]. The higher photocatalytic activities of the prepared nanocomposites than undoped SnO_2 was remarkable observed. In addition, the decrease in the SnO_2 content leads to an increase in the photocatalytic activity as a result of the very low photocatalytic activity of SnO_2 and high photocatalytic activity of ZnO. Moreover, the photocatalyst with 0.1 SnO_2:1.0 ZnO molar ratio is much better than others. This can be ascribed to the configuration of heterojunctions between SnO_2 and ZnO [46,47] as stated above.

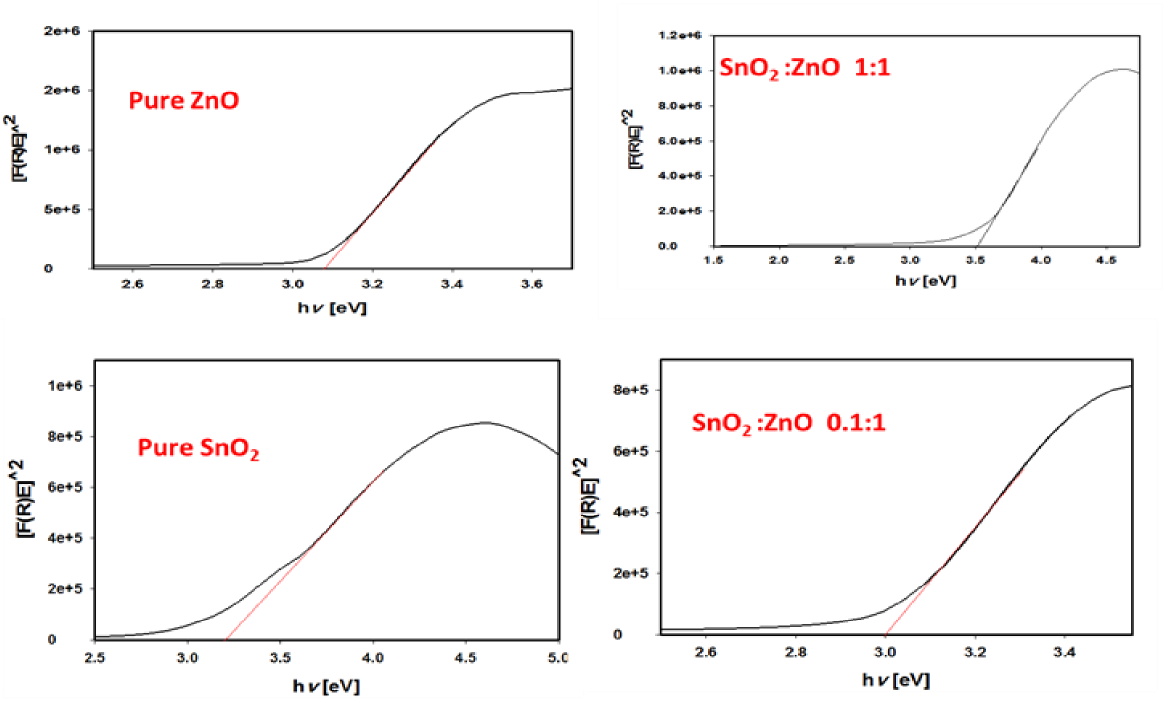

Figure 8. Kubelka-Munk versus energy plots of SnO_2/ZnO.

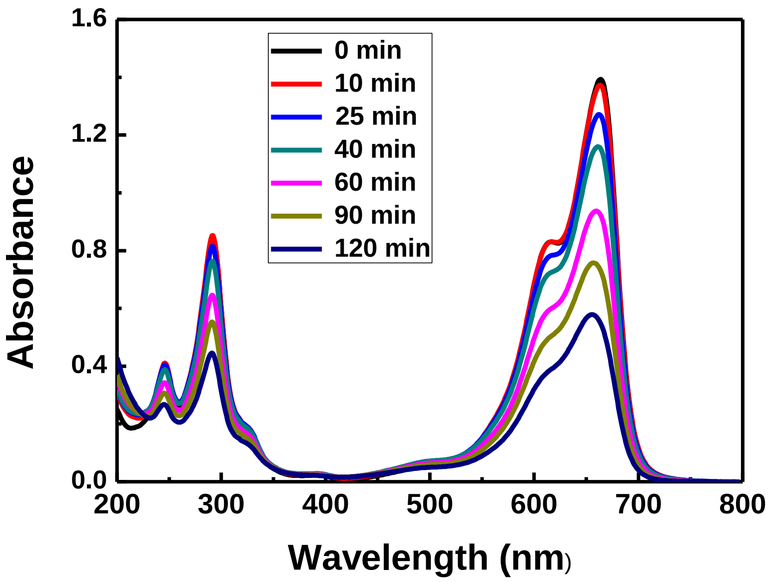

Figure 9. Absorbance vs. wavelength plots with illumination time for SnO_2/ZnO (0.1:1) annealed at 600 °C.

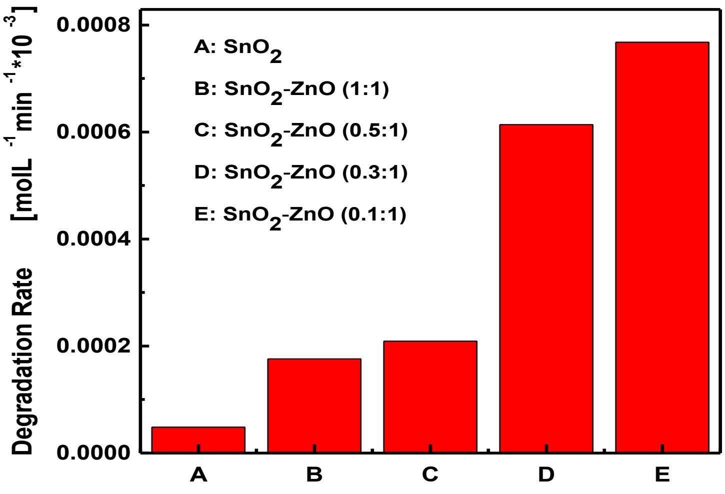

Figure 10. Decomposition of MB in the presence of undoped SnO_2 in SnO_2/ZnO

The photocatalytic action of the undoped nanocomposites for the degradations of MB at different molar ratios is shown in Fig. 11. From figure it is understood that for the (0.1:1.0) SnO_2/ZnO showing high photocatalytic action i.e., 0.1 SnO_2 content, most efficient heterojunction which may be due to effective lowering of e^-/h^+ pair recombination, eventually rising the degradation rate. After that, increase the SnO_2 content leads to a reduce in the photocatalytic activity due to the formation of SnO_2/SnO_2 homojunctions, which reduce the number of SnO_2/ZnO heterojunctions and also increase free SnO_2 nanoparticles possessing a low photocatalytic activity [48]. The decreased band gap of (0.1:1.0) SnO_2/ZnO (Fig. 8) might be due to the other reasons. From the diffuse reflectance spectral results, SnO_2 doping leads to a decrease in the band gap, which can simply be activated by visible light, thus availability of electron and hole pairs grows resulting in the efficient generation of highly active hydroxyl radicals ($OH^•$) and superoxide radical anions ($O_2^{•-}$) for the degradation of target pollutants. Fig. 12 shows the % degradation with respect to irradiation time.

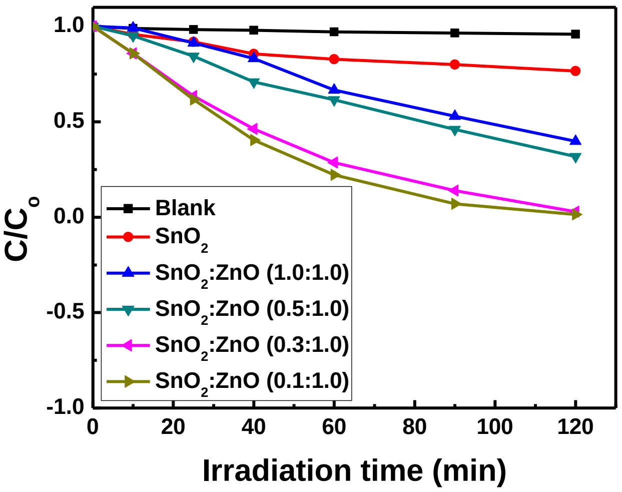

Figure 11. Change in concentration vs. irradiation time at 600 °C.

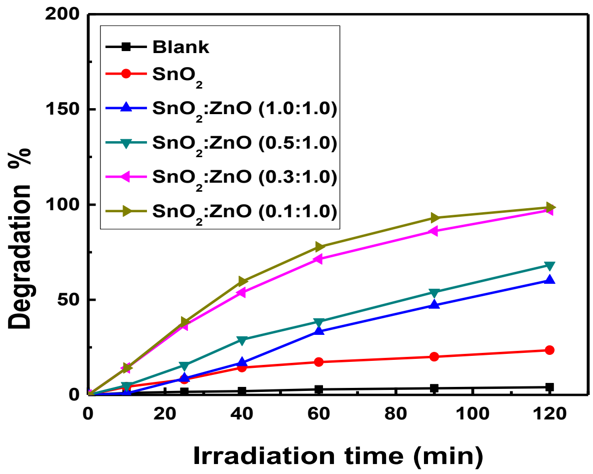

Figure 12. The % degradation vs. irradiation time in the presence of various photocatalysts.

To confirm further the inner structures, the nitrogen adsorption and desorption characterizations of the SnO_2/ZnO at (1.0:1.0) and (0.1:1.0) ratio and 600 °C were performed the properties as depicted in Figs. 13 and 14. The adsorbed amount of N_2 on SnO_2/ZnO (0.1:1.0) is smaller than on that of pure SnO_2, indicating that SnO_2/ZnO (0.1:1.0) has a lower surface area than pure SnO_2. SnO_2/ZnO (0.1:1.0) has a BET surface area of 11.26 m^2/g, which is lower than pure SnO_2 (25.04 m^2/g) (Fig. 15). The size of SnO_2 and ZnO in the SnO_2/ZnO samples is showing smaller values than pure material, which are match with the XRD results. The pure SnO_2 has the total surface area of 25.04 m^2/g. It is much lower than that of the SnO_2 nanoparticles such as SnO_2 (Brunauer-Emmett-Teller (BET) 47.2 m^2/g, 18.3 nm in diameter, No. 549657–25G, Aldrich), SnO_2 (BET 25.9 m^2/g, 34 nm in diameter, Yamanaka & Co. Ltd., Osaka, Japan), and higher than SnO_2 (BET 23 m_2/g, 26 nm in diameter, No. 37314–13, NanoTek, C. I. Kasei Co. Ltd., Tokyo, Japan) [49]. The pore size distribution was analyzed by the Barrett-Joyner-Hanlenda method using adsorption isotherm (inset) (Figs. 13–16).

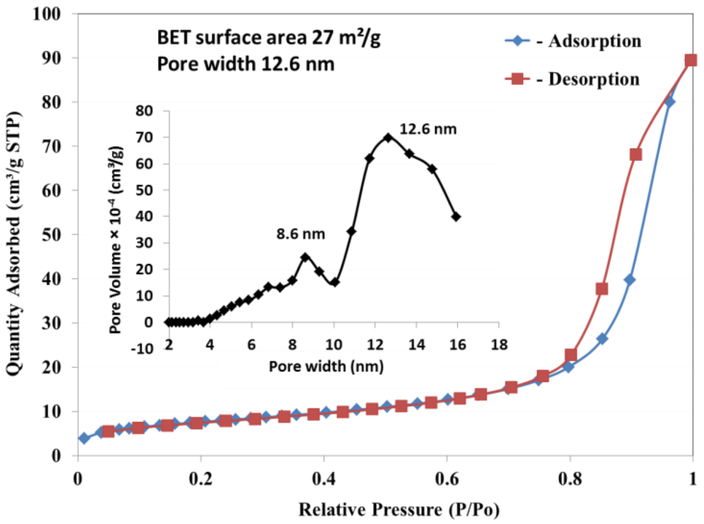

Figure 13. N_2 adsorption isotherms for sample SnO_2/ZnO (1.0:1.0) at 600 °C. Inset is pore size distribution calculated from N_2 adsorption data of SnO_2/ZnO (1.0:1.0) nanocomposite.

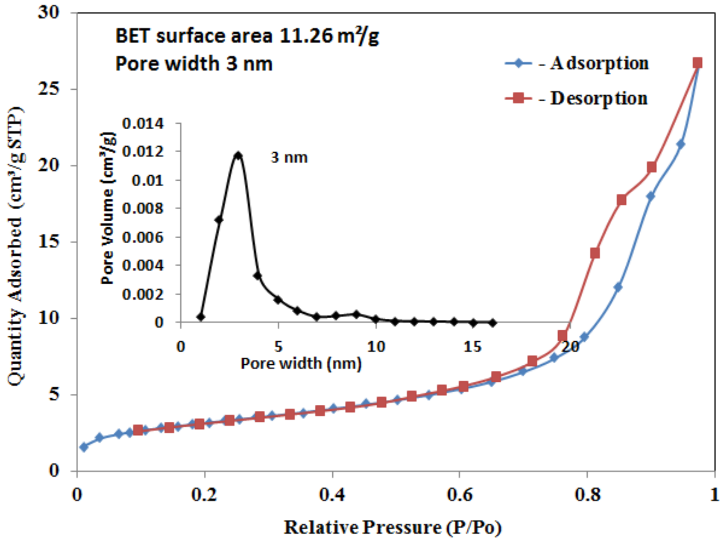

Figure 14. N_2 adsorption isotherms for sample SnO_2/ZnO (0.1:1.0) at 600 °C. Inset is pore size distribution calculated from N_2 adsorption data of SnO_2/ZnO (0.1:1.0) nanocomposite.

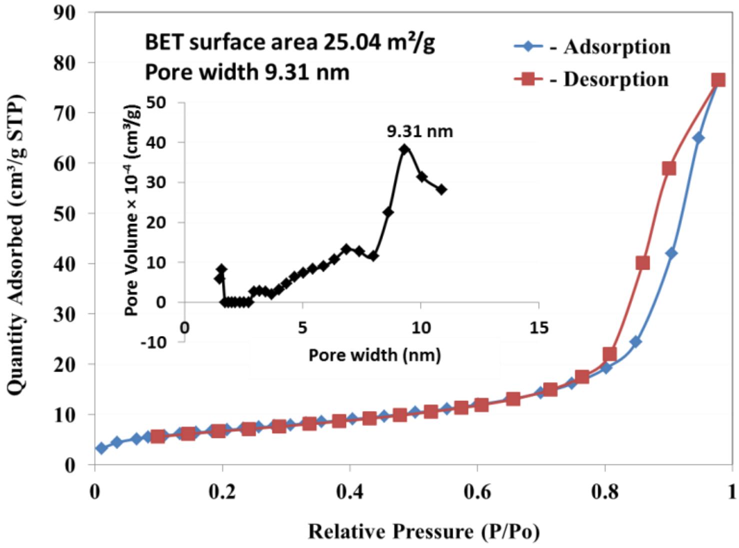

Figure 15. N_2 adsorption isotherms of pure SnO_2 at 600 °C. Pore size distribution calculated from N_2 adsorption data of pure SnO_2 nanocomposite (inset).

Bare, unmodified GCE and SnO_2/ZnO modified GCE were firstly examined for their electrocatalytic activity using the cyclic voltammetry (CV) approach in 0.1M PBS of pH 7.4 containing 0.1 mM hydrazine. The CVs obtained using both electrodes are shown in Fig. 17. As could be seen, bare GCE generates small anodic current starting at ~0.3 V vs Ag/AgCl and reached its maximum value of around 0.5 µA, with no noticeable anodic peak. However, much enhanced anodic current was detected at the SnO_2/ZnO modified GCE and reached to almost three times more current compared to the current induced at bare GCE. The anodic current starts also to appear at a lower over-potential compared to the unmodified GCE (~0.2V), forming a real, distinct anodic peak at ~0.45V (I_{pa}=1.5µA) related to hydrazine elecro-oxidation. This observation ensures that the electro-catalytic activity of the modified electrode was notably promoted compared to unmodified one. Furthermore, a cathodic current was also detected at the SnO_2/ZnO modified GCE due to H_2O molecules reduction. The enhanced increase in the anodic peak current suggests a quicker electron moment and consequently hydrazine can be determined electrochemically via such an oxidation event. The electrochemical oxidation of hydrazine has been studied at various changed electrodes and the oxidation process has been reported to involve a 4-electron transfer, generating N_2 gas in last stage based on the following equations [50-54]:

$$N_2H_4 + H_2O \longrightarrow N_2H_3 + H_3O^+ + e^- \quad \text{(slow step)}$$

$$N_2H_3 + 3H_2O \longrightarrow N_2 + 3H_3O^+ + 3e^- \quad \text{(fast step)}$$

$$N_2H_4 + 4H_2O \rightleftharpoons N_2 + 4H_3O^+ + 4e^- \quad \text{(overall reaction)}$$

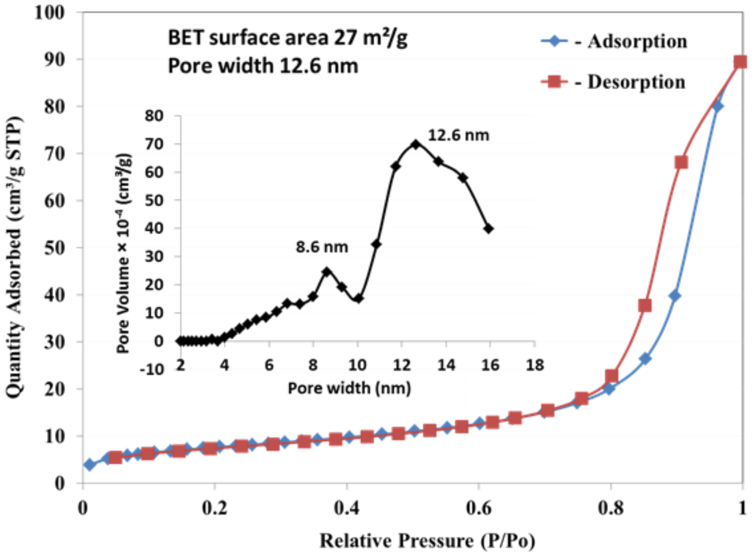

Figure 16. N_2 adsorption isotherms of pure ZnO at 600 °C. Pore size distribution calculated from N_2 adsorption data of pure ZnO nanocomposite (inset).

Finding of hydrazine with different concentrations was examined electrochemically via the amperometric approach at the SnO_2/ZnO modified GCE. The current transient (*i-t)* response is shown in Fig. 18(a). A quick increment of oxidation current was detected upon the successive injection of hydrazine into the stirred buffer solution, reaching its levelling value within ~5 s response time. A typical staircase curve was obtained at the modified working electrode, indicating effective sensing of hydrazine.

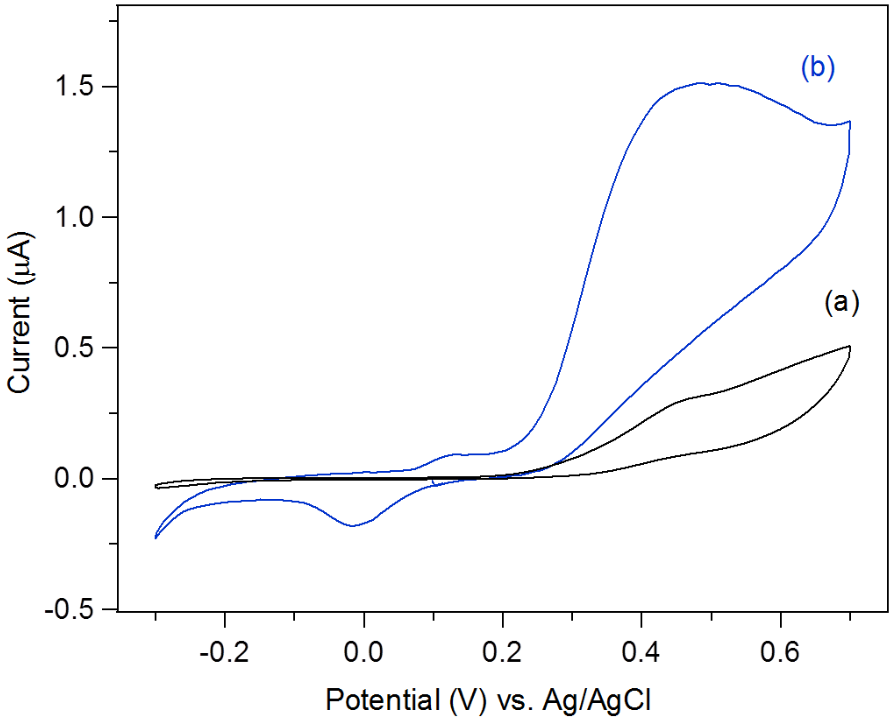

Figure 17. Cyclic voltammetry measure at a scan rate 50 mV/s on bare GCE (a) and SnO_2/ZnO modified GCE (b) in 0.1 M PBS of pH=7.4 containing 0.1 mM hydrazine.

Fig. 18(b) shows the calibration plot drawn using the above *i-t* data. As revealed, the oxidation current is linearly correlated to the injected hydrazine concentration within the examined range between 2.5-25 µM, giving a correlation coefficient R^2=0.9997. The appropriate equation (3) is written as:

$$I\ (\mu A) = 0.0822\ [\text{hydrazine}]\ (\mu A) + 0.0473 \quad (3)$$

The electrode sensitivity could be estimated from the ratio between slope of calibration plot and the electrode area, the obtained sensitivity was 1.16 $\mu A \mu M^{-1} cm^{-2}$. The limit of detection (LOD) is calculated for the current modified electrode based according to equation (4):

$$\text{LOD} = 3\ S_b/m \quad (4)$$

m is the slope of calibration curve (0.0822 $\mu A \mu M^{-1}$) and S_b is the standard deviation and equals to 0.01 µA as measured from average five measurements using a blank sample in buffer solution. The LOD was calculated as 0.36 µM.

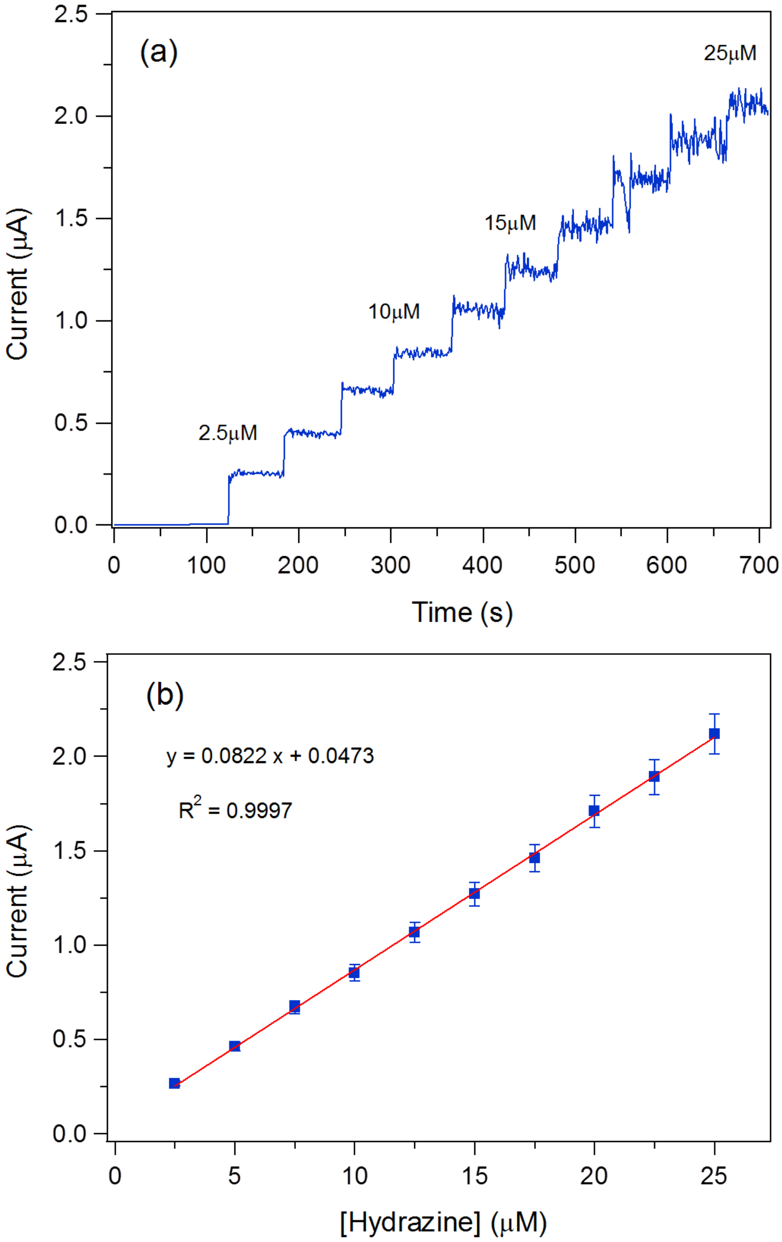

Figure 18. (a) Amperometric detection (*i*-*t* response) of hydrazine measured at a potential 0.45V *vs.* Ag/AgCl using the SnO_2/ZnO modified GCE. Successive injections of hydrazine concentration were performed from 2.5 to 25 µM into stirred solution of 0.1M PBS, pH 7.4. (b) The corresponding calibration plot between hydrazine concentration and anodic current.

4. CONCLUSION

In this report, SnO_2/ZnO material is synthesized by the sol-gel method in the existence of PEG at 600 ^{o}C. The examination of a robust ZnO (101) peak indicated that a high orientation occurs at (110) plane for SnO_2. The SEM images showed that the pure ZnO sample has agglomerated type morphology and the grains attached to each other and formed a cluster and the pure SnO_2 sample shows nanorods morphology. The band gaps (Eg) of ZnO, SnO_2, 1.0 SnO_2:1.0 ZnO, and 0.1 SnO_2:1.0 ZnO, are 3.09, 3.5, and 3.00 eV, respectively. The photocatalysts with 0.1 molar ratios showed higher photocatalytic activities than the others. SnO_2/ZnO (0.1:1.0) showed a BET surface area of 11.26 m^2/g, which is quite less than the pure SnO_2 (25.04 m^2/g).

ACKNOWLEDGEMENTS
The authors extend their appreciation to the Deanship of Scientific Research at King Khalid University for funding this work through research groups program under grant number R.G.P. 2/8/38

References

1. H. H. Kung, *Transition Metal Oxides: Surface Chemistry and Catal.*, 45 (1989) 285.
2. M. Baumer, H. Freund, *Prog. Surf. Sci.*, 61 (1999) 127.
3. M. Fernandez-Garcia, J. C, Conesa, F. Illas, *Surf. Sci.,* 349 (1996) 207.
4. J.A. Rodriguez, S. Chaturvedi, M. Kuhn, *Phys. Chem. B*, 102 (1998) 5511.
5. K. Pan, Y. Lin, P. lee, J. Wa, H. Shlh, *J. Nanomaterials*, 2012 (2012) 1.
6. J.J. Chen, L.Y. Lu, W.Y. Wang, *J. Phys. Chem. C*, 116 (2012) 10841.
7. X.H. Hou, Q.A, Cheng, Y. Bai, W.F. Zhang. *Solid state Ionics*, 181 (2010) 631.
8. D. Chen, J. Xu, B. Liang, X.F. Wang, P.C. Chen, C.W. Zhou, G.Z. Chen, *J. Mater. Chem.*, 21 (2011) 17236.
9. P.S. Lee, Y.H. Lin, Y.S. Chang, J.M. Wu, H.C. Shih, *Thin Solid Films*, 519 (2010) 1749.
10. Y.H. Lin, Y.C. Hsueh, C.C. Wang, J. M. Wu, T.P. Perng, H.C. Shih, *Electrochem. Solid-State Lett.*, 13 (2010) 93.
11. Q. Kuang, Z.Y. Jiang, Z.X. Xie, S.C. Lin, Z.W. Lin, S.Y. Xie, R.B. Huang, L.S. Zheng, *J. Am. Chem. Soc.*, 127 (2005) 11777.
12. X.L. Fu, X.X. Wang, J.L. Long, Z.X. Ding, T. J. Yan, G.Y. Zhang, Z.Z. Zhang, H. X. Lin, X.Z. Fu, *J. Solid State Chem.*, 182 (2009) 517.
13. J.D. Perkins, J.A. delcueto, J.L. Alleman, C. Warmsing, B.M. Keyes, L.M. Gedvials , P.A. Parilla , B. To, D.W. Readey, D.S. Ginley, *Thin Solid Films*, 411 (2002) 152.
14. D.L. Young, H. Moutinho, Y. Yan, T. J. Coutts, *J. Appl. Phys.*, 92 (2002) 310.
15. S.Y. Lee, B.O. Park, *Thin Solid Films*, 484 (2005) 184.
16. E. Holmelund, J. Sohou, S. Tougaard, N.B. Larsen, *Appl. Surf. Sci.*, 197 (2002) 467.
17. G. Zhange, M. Liu, *J. Mater. Sci.*, 34 (1999) 3213.
18. C. Wang, C. Yeh, *Appl. Catal.*, 209 (2001) 1.
19. E. Seker, N. Yasyerli, and C. Lambert, R.H. Hammerle, *Appl. Catal. B*, 37 (2002) 27.
20. R. D. Gonzalez, T. Lopez, R. Gomez, *Catal. Today*, 35 (1997) 293.
21. A.A. Ismail, I.A. Ibrahim, *Appl. Catal. A*, 346 (2008) 200.
22. A. Ayeshamariam , C. Sanjeeviraj, R. Perumal Samy, *J. Photonics Spintronics*, 2 (2013) 4.
23. D. Segets, J. Gradl, R.K. Taylor, V. Vassilev, W. Peukert, *ACS Nano*, 3 (2009) 1703.
24. X. Lou, *J. Sens. Trans. Technol.*, 3 (1991) 1.
25. Z.L. Wang, *ACS Nano*, 2 (2008) 1987.
26. M. Chaari, A. Matoussi, *Phys. B*, 407 (2012) 3441.
27. M.S. Seyed-Dorraji, N. Daneshvar, S. Aber, *Global NEST.*, 11 (2009) 535.
28. M.M. Rashad, A.A. Ismail , I. Osama, I.A. Ibrahim, A.T. Kandil, *Arabian J. Chem.*, 7 (2014) 71.
29. C. Wang, B.Q. Xu, and J. Zhao, *J. Solid State. Chem.*, 178 (2005) 3500.
30. B. Pal, T. Hata, G. Nogami, *J. Mol. Catal. A*, 169 (2001) 147.
31. M.H.H. Mahamooud, A.A. Ismail, M.S.S. Sanad, *Chem. Eng.*, 187 (2012) 96.
32. A.M. Ali, O. Qreshah, A.M. Ismail, F.A. Harraz, H. Algarni, M. Faisal, W.S. Chiu, *Int. J.*

Electrochem. Sci., 13 (2018) 6626.
33. Z. Khodami, A. Nezamzadeh-Ejhieh, *J. Molec. Catal. A*, 409 (2015) 59.
34. B.D. Cullity, S.R. Stock. Elements of x-ray diffraction. third ed. Prentice Hall Inc. New Jersey. (2001) p. 72.
35. K. Nejati, Z. Rezvani, R. Pakizevand. *Nano Lett.*, 1 (2011) 75.
36. A. Ghaderi, S. Abbasi, F. Farahood, *Iranian J. Chem. Eng.*, 12 (2015) 96.
37. N. Ashkenov, B.N. Mbenkum, C. Bundesmann, V. Riede, M. Lorenz, D. Spemann, E.M. Kaidashev, A. Kasic, M. Schubert, M. Grundmann, *J. Appl. Phys.*, 93 (2003) 126.
38. R.S. Katiyar, *J. Phys. C*, 3 (1970) 1087.
39. J.G. Traylor, H.G. Smith, R.M. Nicklow, M.K. Wilkinson, *Phys. Rev. B*, 3 (1971) 3457.
40. A. Dieguez, A.R. Rodriguez, A. Vila, J.R. Morante, *J. Appl. Phys.*, 90 (2001) 1550.
41. P.K. Giri, S. Bhattacharyya, D.K. Singh, R. Kesavamoorthy, B.K. Panigrahi, *J. Appl. Phys.*, 102 (2007) 093515.
42. M. Faisal, A.A. Ibrahim, F.A. Harraz, H. Bouzid, M.S. Al-Assiri, A.A. Ismail, *J. Molecular Catal. A*, 397 (2015) 19.
43. A. Sharma, M.Varshney, S. Kumar, K.D. Verina, R. Kumar, *Nanomater Nanotechnol.*, 1 (2011) 29.
44. L.M. Fang, X.T. Zu, Z.J. Li, S. Zhu, C.M. Liu, L.M. Wang, F. Gao, *J. Mater .Sci. Mater. Electron.*, 19 (2008) 868.
45. C. Wu, L. Shen, H. Yu, Q. Huang, Y.C. Zhang, *Mater. Res. Bull.*, 46 (2011) 1107.
46. C.C. Lin, Y.J. Chiang, *Chem. Eng. J.*, 181–182 (2012) 196.
47. K. Tennakone, J. Bandara, *Appl. Catal. A*, 208 (2001) 335.
48. A. Hamrounia, H. Lachheb, A. Houas, *Mater. Sci. Eng. B*, 178 (2013) 1371.
49. Y. Masuda, T. Ohji, K. Kato, *J. Solid State Chem.*, 189 (2012) 21.
50. M. Faisal, F.A. Harraz, A.E. Al-Salami, S.A. Al-Sayari, A. Al-Hajry, M.S. Al-Assiri, *Mater. Chem. Phys.*, 214 (2018) 126.
51. C. Zhang, G. Wang, Y. Ji, M. Liu, Y. Feng, Z. Zhang, B. Fang, *Sens. Actuators B*, 150 (2010) 247.
52. F.A. Harraz, A.A. Ismail, S.A. Al-Sayari, A. Al-Hajry, M.S. Al-Assiri, *Sens. Actuators B*, 234 (2016) 573.
53. W. Sultana, S. Ghosh, B. Eraiah, *Electroanalysis*, 24 (2012)1869.
54. A. A. Ismail, F.A. Harraz, M. Faisal, A.M. El-Toni, A. Al-Hajry, M.S. Al-Assiri, *Mater. Design*, 109 (2016) 530.